

Published in final edited form as:

Contrast Media Mol Imaging. 2011 September ; 6(5): 332–345. doi:10.1002/cmml.443.

Photoacoustic tomography: fundamentals, advances and prospects

Junjie Yao and Lihong V. Wang*

Optical Imaging Laboratory, Department of Biomedical Engineering, Washington University in St. Louis, Campus Box 1097, One Brookings Drive, St. Louis, MO 63130-4899

Abstract

Optical microscopy has been contributing to the development of life science for more than three centuries. However, due to strong optical scattering in tissue, its *in vivo* imaging ability has been restricted to studies at superficial depths. Advances in photoacoustic tomography (PAT) now allow multiscale imaging at depths from sub-millimeter to several centimeters, with spatial resolutions from sub-micrometer to sub-millimeter. Because of this high scalability and its unique optical absorption contrast, PAT is capable of performing anatomical, functional, molecular and fluid-dynamic imaging at various system levels, and is playing an increasingly important role in fundamental biological research and clinical practice. This Review discusses recent technical progress in PAT and presents corresponding applications. It ends with a discussion of several prospects and their technical challenges.

Keywords

Photoacoustic tomography; photoacoustic microscopy; photoacoustic computed tomography; photoacoustic endoscopy; multiscale imaging; optical absorption contrast

1. Introduction

By zooming in on tiny features, optical microscopy has driven the development of life science. However, no matter how sophisticated the optical microscope, its imaging signal fades exponentially with imaging depth (1,2). As a photon travels through tissue, multiple scattering events eventually lead to randomization of its propagation direction, i.e., photon diffusion, and thus blur the image (3). The mean propagation distance for a photon to diffuse is termed the transport mean free path (TMFP), which is typically 1 mm in tissue (2). No existing optical microscopy technologies can penetrate beyond one TMFP, where many biological processes and diseases occur. Therefore, there is a need for non-invasive *in vivo* imaging with high resolution in deep tissue.

Photoacoustic tomography (PAT), an emerging powerful optical imaging modality using optical absorption contrast and ultrasonic resolution, has broken through the fundamental barrier of one TMFP imaging depth (2,4–9). Most importantly, all the key characteristics of PAT are highly scalable. PAT has become one of the fastest growing fields in biomedical imaging (7). To avoid overlapping with recent Review articles, this Review mostly focuses on progress since the second half of year 2009. It is organized in the following order: (1) fundamentals of the photoacoustic effect and photoacoustic imaging, (2) multiscale PAT systems, based on their image formation mechanisms, (3) anatomical and functional PAT

*Corresponding author: lhwang@biomed.wustl.edu.

using intrinsic contrasts, (4) molecular and chemical PAT using exogenous contrasts, (5) PAT of fluid dynamics, and (6) prospects and challenges for PAT development in the near future.

2. Fundamentals of photoacoustic tomography

Based on the photoacoustic effect, discovered by Alexander G. Bell in 1880 (2), the principle of PAT is illustrated in Fig. 1. Typically, the PA effect starts from a target within tissue irradiated by a short laser pulse. The pulse energy is partially absorbed by the target and converted into heat, which generates a local transient temperature rise, followed by a local pressure rise through thermo-elastic expansion. The pressure propagates as ultrasonic waves, termed PA waves, and is detected by ultrasonic transducers placed outside the tissue. A PA image is then formed by resolving the origins of the ultrasonic waves from their arrival times. Because the PA signal amplitude is proportional to the product of the local absorption coefficient and local fluence, PAT is essentially listening to the optical absorption contrast of tissue. Meanwhile, because PAT uncouples signal generation and detection, the diffused photons also contribute to the resultant PA signals without degrading the signal quality. For biological tissue, because ultrasonic scattering is about two to three orders of magnitude weaker than optical scattering, PAT can achieve high spatial resolution deep in tissue. In addition, unlike other coherent imaging techniques, PAT is speckle free (10).

3. Multiscale photoacoustic tomography systems

From organelles to organs, currently, PAT is the only imaging modality spanning the microscopic and macroscopic worlds. The high scalability of PAT is achieved by trading off imaging resolutions and penetration depths (11). Higher acoustic frequency contributes to higher spatial resolution, but is attenuated more by tissue, thus resulting in a shallower penetration depth, and vice versa. In addition, optical attenuation is another limiting factor for penetration depth, since PA waves are generated only where photons can reach. According to their imaging formation mechanisms, PAT systems can be classified into four categories: raster-scan based photoacoustic microscopy (PAM), inverse-reconstruction based photoacoustic computed tomography (PACT), rotation-scan based photoacoustic endoscopy (PAE), and hybrid PAT systems with other imaging modalities. A thorough side-by-side comparison of different PAT systems can be found in recent Review articles (9,11).

3.1. Raster-scan based photoacoustic microscopy

By using a single focused ultrasonic transducer, usually placed confocally with the irradiation laser beam, PAM forms a 1D image at each position, where the flight time of the ultrasound signal provides depth information. A 3D image is then generated by piecing together the 1D images obtained from raster scanning, and thus no inverse reconstruction algorithm is needed. PAM has two forms, based on its focusing mechanism. In acoustic-resolution photoacoustic microscopy (AR-PAM), the optical focus is usually expanded wider than the acoustic focus, and thus acoustic focusing provides the system resolution [Fig. 2(A)] (12,13). Because the resolution is not affected by optical scattering, by using a focused ultrasonic transducer with a 50-MHz central frequency and a 70% nominal bandwidth, a transverse resolution of 15 μm and axial resolution of 45 μm have been achieved with a maximum penetration depth of 3 mm in live animals. However, to further improve the resolution by increasing the acoustic frequency is quite challenging, because of the strong acoustic attenuation at high frequencies (14). The other form of PAM, termed optical-resolution photoacoustic microscopy (OR-PAM), has an optical focus much tighter than the acoustic focus, and thus the system resolution is provided by optical focusing. Since the optical wavelength is much shorter than the acoustic wavelength, OR-PAM can easily

achieve high spatial resolution, down to the micrometer or even sub-micrometer scale [Fig. 2(B)] (14,15). However, like traditional optical microscopy, OR-PAM generally obeys the one TMFP limitation due to photon scattering, which, however, is still deeper than the acoustic solution mentioned above.

PAM usually suffers from slow imaging speed due to raster scanning. To improve this, different scanning mechanisms have been proposed to replace the traditional mechanical scanning. These include optical scanning using Galvo mirrors (~2 Hz frame rate) (16), mechanical scanning using a voice-coil motor (~15 Hz frame rate) (17), and hybrid scanning with optical scanning on one axis and mechanical scanning on the other axis (~6 Hz frame rate) (18).

3.2. Inverse-reconstruction based photoacoustic computed tomography

Despite its high spatial resolution and improved imaging speed, PAM usually has a limited focal depth and is not yet capable of video-rate imaging (19). In contrast, PACT is typically implemented using full-field illumination and a multi-element ultrasound array system to improve penetration depth and imaging speed [Fig. 3(A)] (20–24), though some PACT systems use a single-element transducer with circular scanning [Fig. 3(B)] (25). The spatial distribution of acoustic sources needs to be inversely reconstructed. The ultrasound array can be fabricated in different geometrical forms such as circular (20), semi-circular (23), quarter-circular (26), hemisphere (24), linear (22), and square (27), depending on the application. Mainly determined by the laser repetition rate and data acquisition speed, PACT has been reported with a cross-sectional frame rate of up to 50 Hz (11). Meanwhile, the penetration depth can reach several tens of TMFPs in live tissue. The imaging resolution is usually compromised to several hundreds of micrometers due to the low ultrasound frequency used.

In addition to PACT implementations using piezoelectric ultrasonic transducers, there has been a growing interest in detecting PA signals using optical methods (28–32). Optical detection can potentially improve the imaging sensitivity and eliminate the coupling medium between the sample surface and the ultrasonic transducer (28,31).

3.3. Rotation-scan based photoacoustic endoscopy

Even though the penetration depth of PACT can reach several centimeters, internal organs such as the cardiovascular system and gastrointestinal tract are still not reachable. Non-invasive tomographic imaging of these internal organs is extremely useful in clinical practice. Besides pure optical and ultrasound endoscopy (33–35), photoacoustic endoscopy (PAE) is another promising solution for this clinical need (6). The key specifications of PAE are the probe dimensions and imaging speed. The first PAE was designed by Yang et al., and applied to animal studies (Fig. 4) (36). Here, the PAE probe has a diameter of 4.2 mm and the cross-sectional scanning speed is 2.6 Hz.

3.4. Photoacoustic tomography integrated with other imaging modalities

Combining complementary contrasts can potentially improve diagnostic accuracy. Because of its excellent optical absorption contrast, PAT has been integrated into various imaging modalities, such as ultrasound (US) imaging (mechanical contrast) [Fig. 5(A)] (17,37,38), OCT (optical scattering contrast) [Fig. 5(B)] (39–41), confocal microscopy (scattering/fluorescence contrast) (42–44), two-photon microscopy (fluorescence contrast) (45), and MRI (magnetic contrast) (46). Different modalities in hybrid systems usually share the same imaging area, thus their images are inherently co-registered.

4. Anatomical and functional photoacoustic tomography using intrinsic contrasts

Theoretically, any intrinsic chromophore that has an optical absorption signature can potentially provide PAT contrast, as long as appropriate irradiation wavelengths are applied and the system sensitivity is sufficient. Here, we review the currently used intrinsic contrasts, in the order of hemoglobin, melanin, water, lipid, and nucleic acid.

4.1. Photoacoustic tomography of hemoglobin

In the visible spectral range (450–600 nm), oxyhemoglobin (HbO₂) and deoxyhemoglobin (HbR) account for most of the optical absorption in blood (47). The absorption coefficient ratio between blood and surrounding tissues is as high as six orders of magnitude; hence, PAT can image with nearly no background RBC-perfused vasculature, the functional vascular subset responsible for tissue oxygen supply. Furthermore, because PA signal amplitudes depend on the concentrations of HbO₂ (C_{ox}) and HbR (C_{de}), spectroscopic measurements can be performed to quantify C_{ox} and C_{de} by solving linear equations (48). From C_{ox} and C_{de}, the total hemoglobin concentration (HbT) and oxygen saturation of hemoglobin (sO₂) can be derived. Alternatively, HbT and sO₂ can also be recovered by analyzing the acoustic spectrum (49).

4.1.1. Whole-body photoacoustic tomography of small animals—Small animals, especially mice, are extensively used in preclinical research on human diseases (50,51). Non-invasive whole-body imaging of small animals with high spatial resolution is extremely desirable for systemic studies of such as tumor metastases (52), drug delivery (53), and embryonic development (54).

Laufer et al. have recently reported whole-body images of the vasculature of transgenic mouse embryos, using Fabry-Perot interferometer (FPI)-based PACT [Fig. 6(A)] (30). The vasculature of the head, heart, and spinal cord is clearly visible. This work may enable longitudinal studies of the effects of genetic knockouts on the development of vascular malformations. Brecht et al. reported the first *in vivo* whole-body PAT images of a mouse [Fig. 6(B)] (23). The 3D tomography clearly shows blood-rich internal organs such as the liver, spleen, and kidneys, as well as large and small vasculature. Buehler et al. developed a novel PAT scanner capable of fast whole-body imaging *in vivo* (55). The system has achieved cross-sectional animal imaging with video-rate data acquisition. Imaging performance was demonstrated by resolving the mouse kidney anatomy, which was congruent with the corresponding histological results [Figs. 6(C–E)].

4.1.2. Photoacoustic tomography of human breast—As the leading cause of cancer death among women, breast cancer can be diagnosed earlier by periodic screening (56). Currently, X-ray mammography is the only tool used for mass screening, and it has helped to increase the survival rate of breast cancer patients (57). However, in addition to the accumulation of ionizing radiation dose during lifetime screening, mammography also suffers from low sensitivity for early stage tumors in young women (58). To solve these problems, non-ionizing-radiation based techniques have been investigated, such as ultrasound, MRI, and PAT (24,59,60). Among these techniques, PAT is superior in contrast, sensitivity, and cost effectiveness. The PAT contrast is contributed by the angiogenesis-associated microvasculature around and within the tumor.

Ermilov et al. have used PAT to image breast cancer in humans (60). They imaged single breast slices in craniocaudal or mediolateral projection with at least 0.5 mm resolution. Fig. 7 shows an example of the superior contrast of PAT breast cancer imaging over X-ray

mammography on a radiologically dense breast. A poorly differentiated infiltrating carcinoma can hardly be localized in the mammography image, but it can be easily visualized in the PAT image, with well-defined boundaries. Statistically, preliminary clinical studies demonstrated that PAT was able to visualize 18 malignant tumors out of 20 detected by biopsy, while X-ray mammography only detected 14 of them.

4.1.3. High-resolution functional photoacoustic tomography of

microvasculature—Microvasculature, the distal portion of the cardiovascular system, delivers oxygen, humoral agents, and nutrients to the surrounding tissue and collects metabolic waste (61). Almost any microvasculature-associated parameter has important pathophysiological indications. PAT is highly desirable for microvasculature imaging because of its high spatial resolution and endogenous hemoglobin absorption contrast (11). Three representative applications are introduced here.

Non-invasive, high-resolution PAT of mouse brain activity may help to understand the human neurological diseases. Mouse cortical vasculature and vessel-by-vessel sO_2 mapping obtained by OR-PAM are shown in Figs. 8(A) and (B), respectively (9,62). Major vascular landmarks can be well identified. The strong capability of PAT for functional brain imaging will greatly advance neurological studies.

Many eye diseases are associated with altered eye microvasculature. So far, PAT has been demonstrated to be safe for ocular and retinal microvasculature imaging in small animals [Figs. 8(C–D)] (39,63–66). All the major vascular components can be clearly visualized under the ANSI safety standard for the eye. sO_2 in the iris microvasculature is also imaged spectrally. PAT offers significant promise for radiation-free monitoring of eye diseases.

Anti-angiogenesis is an important cancer treatment strategy (67). PAT is an ideal tool for angiogenesis-associated studies and has been applied to various tumor models, such as melanoma, glioblastoma, adenocarcinoma, carcinoma, and gliosarcoma (8). Fig. 8(E) shows an implanted human colorectal adenocarcinoma LS174T imaged by FPI-PACT (31). The image reveals a poorly and heterogeneously vascularized tumor core supplied by larger vessels around its periphery, which is a known feature of this type of tumor. PAT characterization of tumor vasculature will aid the development and refinement of new cancer therapies.

4.2. Photoacoustic tomography of melanin

Although it is the foremost killer among skin cancers, melanoma can be cured if detected early (68). PAT has been investigated for non-invasive melanoma imaging using melanin, the light-absorbing molecules in melanosomes, as the contrast (12,15,69,70). The absorption of melanin is ~1000 times that of water at 700 nm, which can potentially enable PAT to detect early melanoma in deep tissue.

Fig. 9(A) shows the blood vessels (in red) and melanoma (in brown) in the ear of a nude mouse imaged by OR-PAM (15). The melanoma generated stronger PA signals than the vessels and can be easily identified from the blood vessels by taking the difference before and after the injection of tumor cells. Because of the high scalability of PAT, the spatial resolution can be scaled down to sub-micrometer for single melanoma cell imaging by using an optical objective with higher NA [Fig. 9(B)] (15), or scaled up to sub-millimeter for brain melanoma growth monitoring with intact skull and scalp by changing to acoustic resolution [Fig. 9(C)] (69).

4.3. Photoacoustic tomography of water

Water is the most abundant chemical in human body (57% of the body weight) (71). The body water content can reflect a disease state. Because water has much stronger absorption than other tissue components in the spectral range between 920 to 1040 nm (72), PAT is a promising tool to provide high resolution water imaging with high sensitivity. Fig. 10 shows the first PAT water imaging in a tissue phantom (73). First, spectral measurements of water-ethanol mixtures demonstrate that water concentration can be resolved by multi-wavelength excitation [Fig. 10(A)]. Second, a tissue phantom (2% agar embedded in fat) experiment at 975 nm shows that PAT can be used for water detection at low concentration, such as in fat [Figs. 10(B–C)]. *In vivo* PAT water imaging is expected in the near future.

4.4. Photoacoustic tomography of lipid

Cardiovascular disease (CVD) has been the number one cause of death in the United States for over a century. The majority of CVD is due to atherosclerosis, characterized by plaques building up inside the arterial wall (74). Lipid is a common constituent in atherosclerotic plaques, the location and area of which are closely related to the progression of the disease. PAT is well suited for lipid imaging: compared with water-based tissue components, lipid has a distinct absorption spectrum between 1150 nm and 1250 nm [Fig. 11(A)] (75–77). A recent advance in PAT lipid imaging was reported by Allen et al. (77). A human aorta containing a raised lipid-rich plaque [Fig. 11(B)] was imaged at 1200 nm [Fig. 11(C)]. The plaque is clearly identified due to the strong absorption by lipid. The results demonstrate that spectroscopic PAT is a promising tool for lipid detection in atherosclerosis.

4.5. Photoacoustic tomography of cell nuclei

Cell nuclei are organelles where major cell activities take place. Compared with those of normal cells, nuclei of cancer cells have folded shapes and enlarged size (78). Imaging cell nuclei plays a critical role in cancer diagnosis. Traditional imaging of cell nuclei needs tissue sectioning and histological staining, which are not applicable for *in vivo* studies. Because nucleic acids, the major components of DNA and RNA in cell nuclei, have strong absorption in the ultraviolet range (79), PAT is a good choice for imaging of cell nuclei using nucleic acids as intrinsic contrast.

By exciting DNA and RNA at 266 nm, Yao et al. have recently reported the first label-free PA *ex vivo* and *in vivo* images of cell nuclei (Fig. 12) (80), termed UV-PAM. Cell nuclei in the epithelia of the mouse lip and the intestinal villi were imaged *ex vivo* [Figs. 12(A–B)]. Cell nuclei in the ear skin of a nude mouse were imaged *in vivo* at depths greater than 100 μm [Fig. 12(C)]. UV-PAM is capable of 3D noninvasive cell nuclei imaging without staining.

5. Chemical and molecular photoacoustic tomography using exogenous contrast agents

Even though the intrinsic contrasts in biological tissue are promising, exogenous contrast agents can extend the power of PAT. So far, optically absorptive organic dyes, nanoparticles, reporter genes (81), fluorescent proteins, microbubbles, and nanobubbles (82) have been successfully applied to PAT imaging. A thorough discussion of these agents can be found in a recent Review article (8), and only a few new applications are presented here.

Organic dyes, such as indocyanine green (ICG), IRDye800-NHS, methylene blue (MB), Evans blue (EB), and Congo red are widely used in PAT applications, including brain cortical structure enhancement (83), kidney perfusion (55), brain hemodynamic monitoring (20), tumor targeting (84), sentinel lymph node (SLN) mapping (37,38,85), capillary enhancement (86), and amyloid plaque staining (87). These dyes usually have peak

absorption wavelengths within the near-infrared range, where blood and water have weak absorption; hence, the penetration depth can be improved. Fig. 13 shows an example of SLN mapping using MB as the contrast (38). An imaging depth of greater than 2 cm was demonstrated. This study is an important step towards the clinical translation of PAT. In addition to increasing the penetration depth, when conjugated with other functional ligands, organic dyes can specifically target cellular sites of interest, such as tumor cell membranes.

Nanoparticles are of great research interest in PAT applications, and they have proven effective in delivering therapeutic agents by targeting specific sites (88,89). Because the properties of nanoparticles are highly size-dependent, their absorption spectra can be optimized by adjusting the particle geometry and dimensions, which makes them more flexible than organic dyes (8). In addition, targeted nanoparticles can significantly improve the imaging specificity of PAT (90). So far, different kinds of nanoparticles, including nanocages, nanoshells, nanorods, nanotubes, nanobeacons, and nanowontons, have been explored as PAT contrasts for different applications, such as cerebral cortex imaging (91), SLN mapping (92), macrophage imaging in atherosclerosis (93), and solid tumor targeting (94). Nanoparticle enhanced PAT has become a hot topic in biomedical studies.

As fluorescent proteins have totally redefined the ways in which biologists investigate the cellular and subcellular progress, deep fluorescent protein imaging by PAT has extended the ways we use these proteins (4,81,95). The multispectral PAT technique is capable of detecting fluorescent proteins within highly light-scattering organisms (81,96). Razansky et al. showed the feasibility of resolving tissue-specific expression of mCherry proteins *in vivo* (25). As shown in Fig. 14, whole-body spectroscopic PA imaging was performed on an adult zebra fish. The location of mCherry expression was accurately resolved [Fig. 14(D); red corresponds to the mCherry-expressing vertebral column]. The PAT image resolution is better than 40 μm at depth >1 mm, while confocal microscopy can hardly penetrate 500 μm [Fig. 14(G)].

6. Photoacoustic tomography of fluid dynamics

Flow, an important contrast for biomedical imaging, provides much useful pathophysiological information. PAT is receiving increased attention as a tool to measure flow, as in PAT flowmetry. PAT flowmetry keeps all the merits of PAT and can perform better than scattering-based optical flowmetries in deep tissue.

So far, several principles have been proposed for PA measurement of flow. Fang et al. discovered the photoacoustic Doppler effect (PAD), and used an intensity-modulated CW laser to measure the flow speed based on the PAD frequency shift (97). Sheinfeld et al. extended this method by using pulsed sinusoidal (burst) excitation to attain axial information (98). Brunner et al. quantified the Doppler time shifts via cross-correlation of pairs of photoacoustic waveforms to measure the flow speed (99). Wei et al. extracted flow information based on rod-to-sphere shape transformations of gold nanorods induced by pulsed-laser irradiation (100). Fang et al. invented M-mode particle flowmetry by measuring the traveling time of absorptive particles across the optical illumination area (101). Yao et al. have reported a transverse flow imaging strategy on the basis of Doppler bandwidth broadening [Fig. 15(A)] (102,103). Using this method, the blood flow of an artery-vein pair in a mouse ear was imaged [Fig. 15(B)]. Chen et al. demonstrated a similar idea but conducted the analysis via auto-correlation in the time domain (104).

7. Prospects and summary

From organelles to whole bodies, from superficial microvasculature to internal organs, from anatomy to functions, PAT is playing an increasingly important role in basic physiological

research and pre-clinical studies. Exciting events are happening in this fast growing field. Several prospects and corresponding challenges are discussed here.

Integration of the state-of-the-art techniques in system implementation will eventually lead PAT to commercialization for clinical practice. For PAM, a fast scanning mechanism and a high repetition rate laser with a wide tuning range of wavelengths are necessary for real-time functional imaging without compromising the spatial resolution. Also, a better optical and acoustic focusing method is needed to maintain the resolution in the depth dimension. For PACT, new techniques for assembling ultrasound arrays help to increase the imaging sensitivity and improve the spatial resolution (105). More homogeneous beam expansion over the sample surface is necessary for whole-field illumination. Parallel, real-time data acquisition is also important for further improving the imaging speed. For PAE, time gating may be necessary for eliminating motion artifacts induced by heart beating and breathing. Moreover, element minimization can still be improved to reduce the probe size to less than 1 mm in diameter. For PAT systems integrated with other modalities, multimodal contrast agents show great promise in providing complementary information (106).

Robust, fast, and automatic data processing will greatly enhance PAT performance. Currently, different inverse reconstruction methods have been used to improve PAT image quality, such as compressed-sensing (107), deconvolution (108), and wavelet filtering (109) based algorithms. However, each method usually works well only under some specific conditions, and the 3D reconstruction speed is usually too slow for clinical usage. In addition, the heterogeneity of optical fluence and sound speed distribution within the imaged plane may also degrade the reconstructed image. Therefore, a fast, quantitative, universally applicable image reconstruction algorithm is desirable. Besides image reconstruction, pre-processing of raw data and postprocessing of reconstructed images are also important. The former can help image reconstruction by de-noising and data compressing, while the latter can aid physicians in analyzing the results and thus making better diagnosis.

New imaging principles will be explored using PAT. In the PA effect, as irradiation intensity increases, mechanisms such as saturation of the optical absorption or multiphoton/multistep absorption can occur, resulting in a nonlinear dependence of the photoacoustic signal on the excitation pulse fluence (110,111). Danielli et al. recently reported a relaxation photoacoustic microscopy (rPAM) (111). From the saturation of the optical absorption, picosecond relaxation times of different chromophores were measured using nanosecond laser pulses. Nonlinear photoacoustic tomography will potentially become an interesting direction.

New parameters can be measured by PAT. For example, by combining the oxyhemoglobin concentration and volumetric blood flow, the metabolic rate of oxygen can be computed in the region of interest (6). Moreover, if the blood glucose concentration is also measured by PAT, aerobic and anaerobic metabolism of glucose can be quantified, respectively, which will be extremely useful for cancer diagnosis and treatment evaluation.

In summary, photoacoustic tomography perfectly complements other biomedical imaging modalities by providing unique optical absorption contrast with highly scalable spatial resolution, penetration depth, and imaging speed. In light of its capabilities and flexibilities, PAT is expected to play a more essential role in biomedical studies and clinical practice.

Acknowledgments

The authors thank Prof. James Ballard for manuscript editing. This research was supported by the National Institutes of Health Grants R01 EB000712, R01 EB008085, R01 CA134539, U54 CA136398, R01 EB010049, and

5P60 DK02057933. L.V.W. has financial interest in Microphotoacoustics, Inc. and Endra, Inc., which, however, did not support this work.

References

1. Webb RH. Theoretical basis of confocal microscopy. *Method Enzymol.* 1999; 307:3–20.
2. Wang, LV.; Wu, H-i. *Biomedical optics: principles and imaging.* Hoboken, N.J: Wiley-Interscience; 2007. p. xivp. 362
3. Beauvoit B, Evans SM, Jenkins TW, Miller EE, Chance B. Correlation between the Light-Scattering and the Mitochondrial Content of Normal-Tissues and Transplantable Rodent Tumors. *Anal Biochem.* 1995; 226(1):167–174. [PubMed: 7785769]
4. Ntziachristos V. Going deeper than microscopy: the optical imaging frontier in biology. *Nat Methods.* 2010; 7(8):603–614. [PubMed: 20676081]
5. Wang LV. Tutorial on photoacoustic microscopy and computed tomography. *Ieee J Sel Top Quant.* 2008; 14(1):171–179.
6. Wang LV. Prospects of photoacoustic tomography. *Med Phys.* 2008; 35(12):5758–5767. [PubMed: 19175133]
7. Wang LV. Multiscale photoacoustic microscopy and computed tomography. *Nat Photonics.* 2009; 3(9):503–509. [PubMed: 20161535]
8. Kim C, Favazza C, Wang LHV. In Vivo Photoacoustic Tomography of Chemicals: High-Resolution Functional and Molecular Optical Imaging at New Depths. *Chem Rev.* 2010; 110(5):2756–2782. [PubMed: 20210338]
9. Hu S, Wang LV. Neurovascular photoacoustic tomography. *Front Neuroenergetics.* 2010; 2:10. [PubMed: 20616885]
10. Guo ZJ, Li L, Wang LHV. On the speckle-free nature of photoacoustic tomography. *Med Phys.* 2009; 36(9):4084–4088. [PubMed: 19810480]
11. Hu S, Wang LV. Photoacoustic imaging and characterization of the microvasculature. *J Biomed Opt.* 2010; 15(1):011101. [PubMed: 20210427]
12. Zhang HF, Maslov K, Stoica G, Wang LHV. Functional photoacoustic microscopy for high-resolution and noninvasive in vivo imaging. *Nat Biotechnol.* 2006; 24(7):848–851. [PubMed: 16823374]
13. Maslov K, Stoica G, Wang LHV. In vivo dark-field reflection-mode photoacoustic microscopy. *Opt Lett.* 2005; 30(6):625–627. [PubMed: 15791997]
14. Maslov K, Zhang HF, Hu S, Wang LV. Optical-resolution photoacoustic microscopy for in vivo imaging of single capillaries. *Opt Lett.* 2008; 33(9):929–931. [PubMed: 18451942]
15. Zhang C, Maslov K, Wang LHV. Subwavelength-resolution label-free photoacoustic microscopy of optical absorption in vivo. *Opt Lett.* 2010; 35(19):3195–3197. [PubMed: 20890331]
16. Xie ZX, Jiao SL, Zhang HF, Puliafito CA. Laser-scanning optical-resolution photoacoustic microscopy. *Opt Lett.* 2009; 34(12):1771–1773. [PubMed: 19529698]
17. Harrison, T.; Ranasinghesagara, J.; Lu, H.; Zemp, RJ. Fast-scanning ultrasonic-photoacoustic biomicroscope: in vivo performance. Oraevsky, AA.; Wang, LV., editors. San Francisco, California, USA: SPIE; 2010. p. 75641X-75647.
18. Rao B, Li L, Maslov K, Wang LH. Hybrid-scanning optical-resolution photoacoustic microscopy for in vivo vasculature imaging. *Opt Lett.* 2010; 35(10):1521–1523. [PubMed: 20479795]
19. Zhang HF, Maslov K, Wang LHV. Automatic algorithm for skin profile detection in photoacoustic microscopy. *J Biomed Opt.* 2009; 14(2):024050. [PubMed: 19405778]
20. Li CH, Aguirre A, Gamelin J, Maurudis A, Zhu Q, Wang LV. Real-time photoacoustic tomography of cortical hemodynamics in small animals. *J Biomed Opt.* 2010; 15(1):010509. [PubMed: 20210422]
21. Gamelin J, Maurudis A, Aguirre A, Huang F, Guo PY, Wang LV, Zhu Q. A real-time photoacoustic tomography system for small animals. *Opt Express.* 2009; 17(13):10489–10498. [PubMed: 19550444]

22. Song LA, Maslov K, Shung KK, Wang LHV. Ultrasound-array-based real-time photoacoustic microscopy of human pulsatile dynamics in vivo. *J Biomed Opt.* 2010; 15(2):021303. [PubMed: 20459225]
23. Brecht HP, Su R, Fronheiser M, Ermilov SA, Conjusteau A, Oraevsky AA. Whole-body three-dimensional optoacoustic tomography system for small animals. *J Biomed Opt.* 2009; 14(6): 064007. [PubMed: 20059245]
24. Kruger R, Lam R, Reinecke D, Del Rio S, Doyle R. Photoacoustic angiography of the breast. *Med Phys.* 2010; 37(11):6096–6100. [PubMed: 21158321]
25. Razansky D, Distel M, Vinegoni C, Ma R, Perrimon N, Koster RW, Ntziachristos V. Multispectral opto-acoustic tomography of deep-seated fluorescent proteins in vivo. *Nat Photonics.* 2009; 3(7): 412–417.
26. Gamelin J, Aguirre A, Maurudis A, Huang F, Castillo D, Wang LV, Zhu Q. Curved array photoacoustic tomographic system for small animal imaging. *J Biomed Opt.* 2008; 13(2):024007. [PubMed: 18465970]
27. Balogun O, Regez B, Zhang HF, Krishnaswamy S. Real-time full-field photoacoustic imaging using an ultrasonic camera. *J Biomed Opt.* 2010; 15(2):021318. [PubMed: 20459240]
28. Payne BP, Venugopalan V, Mikic BB, Nishioka NS. Optoacoustic tomography interferometric detection using time-resolved of surface displacement. *J Biomed Opt.* 2003; 8(2):273–280. [PubMed: 12683854]
29. Nuster R, Holotta M, Kremser C, Grossauer H, Burgholzer P, Paltauf G. Photoacoustic microtomography using optical interferometric detection. *J Biomed Opt.* 2010; 15(2):021307. [PubMed: 20459229]
30. Laufer, JG.; Cleary, JO.; Zhang, EZ.; Lythgoe, MF.; Beard, PC. Photoacoustic imaging of vascular networks in transgenic mice. Oraevsky, AA.; Wang, LV., editors. San Francisco, California, USA: SPIE; 2010. p. 75641A-75645.
31. Zhang EZ, Laufer JG, Pedley RB, Beard PC. In vivo high-resolution 3D photoacoustic imaging of superficial vascular anatomy. *Phys Med Biol.* 2009; 54(4):1035–1046. [PubMed: 19168938]
32. Zhang E, Laufer J, Beard P. Backward-mode multiwavelength photoacoustic scanner using a planar Fabry-Perot polymer film ultrasound sensor for high-resolution three-dimensional imaging of biological tissues. *Appl Optics.* 2008; 47(4):561–577.
33. Sergeev A, Gelikonov V, Gelikonov G, Feldchtein F, Kuranov R, Gladkova N, Shakhova N, Snopova L, Shakhov A, Kuznetzova I, Denisenko A, Pochinko V, Chumakov Y, Streltsova O. In vivo endoscopic OCT imaging of precancer and cancer states of human mucosa. *Opt Express.* 1997; 1(13):432–440. [PubMed: 19377567]
34. Kiesslich R, Burg J, Vieth M, Gnaendiger J, Enders M, Delaney P, Polglase A, McLaren W, Janell D, Thomas S, Nafe B, Galle PR, Neurath MF. Confocal laser endoscopy for diagnosing intraepithelial neoplasias and colorectal cancer in vivo. *Gastroenterology.* 2004; 127(3):706–713. [PubMed: 15362025]
35. Rosch T, Lorenz R, Braig C, Feuerbach S, Siewert JR, Schusdzarra V, Classen M. Endoscopic Ultrasound in Pancreatic Tumor-Diagnosis. *Gastrointest Endosc.* 1991; 37(3):347–352. [PubMed: 2070987]
36. Yang JM, Maslov K, Yang HC, Zhou QF, Shung KK, Wang LHV. Photoacoustic endoscopy. *Opt Lett.* 2009; 34(10):1591–1593. [PubMed: 19448831]
37. Kim C, Erpelding TN, Jankovic L, Pashley MD, Wang LV. Deeply penetrating in vivo photoacoustic imaging using a clinical ultrasound array system. *Biomed Opt Express.* 2010; 1(1): 278–284. [PubMed: 21258465]
38. Erpelding TN, Kim C, Pramanik M, Jankovic L, Maslov K, Guo Z, Margenthaler JA, Pashley MD, Wang LV. Sentinel lymph nodes in the rat: noninvasive photoacoustic and US imaging with a clinical US system. *Radiology.* 2010; 256(1):102–110. [PubMed: 20574088]
39. Li L, Maslov K, Ku G, Wang LV. Three-dimensional combined photoacoustic and optical coherence microscopy for in vivo microcirculation studies. *Opt Express.* 2009; 17(19):16450–16455. [PubMed: 19770860]

40. Jiao SL, Xie ZX, Zhang HF, Puliafito CA. Simultaneous multimodal imaging with integrated photoacoustic microscopy and optical coherence tomography. *Opt Lett*. 2009; 34(19):2961–2963. [PubMed: 19794782]
41. Zhang, EZ.; Laufer, J.; Povazay, B.; Alex, A.; Hofer, B.; Drexler, W.; Beard, P. Multimodal simultaneous photoacoustic tomography, optical resolution microscopy, and OCT system. Oraevsky, AA.; Wang, LV., editors. San Francisco, California, USA: SPIE; 2010. p. 75640U-75647.
42. Zhang X, Jiang M, Fawzi AA, Li X, Shung KK, Puliafito CA, Zhang HF, Jiao S. Simultaneous dual molecular contrasts provided by the absorbed photons in photoacoustic microscopy. *Opt Lett*. 2010; 35(23):4018–4020. [PubMed: 21124598]
43. Wang Y, Maslov K, Kim C, Hu S, Wang LHV. Integrated Photoacoustic and Fluorescence Confocal Microscopy. *Ieee T Bio-Med Eng*. 2010; 57(10):2576–2578.
44. Zhang HF, Wang J, Wei Q, Liu T, Jiao SL, Puliafito CA. Collecting back-reflected photons in photoacoustic microscopy. *Opt Express*. 2010; 18(2):1278–1282. [PubMed: 20173952]
45. van Raaij, ME.; Lee, M.; Cherin, E.; Stefanovic, B.; Foster, FS. Femtosecond photoacoustics: integrated two-photon fluorescence and photoacoustic microscopy. Oraevsky, AA.; Wang, LV., editors. San Francisco, California, USA: SPIE; 2010. p. 75642E-75646.
46. Bouchard LS, Anwar MS, Liu GL, Hann B, Xie ZH, Gray JW, Wang XD, Pines A, Chen FF. Picomolar sensitivity MRI and photoacoustic imaging of cobalt nanoparticles. *P Natl Acad Sci USA*. 2009; 106(11):4085–4089.
47. Wang XD, Xie XY, Ku GN, Wang LHV. Noninvasive imaging of hemoglobin concentration and oxygenation in the rat brain using high-resolution photoacoustic tomography. *J Biomed Opt*. 2006; 11(2):024015. [PubMed: 16674205]
48. Zhang HF, Maslov K, Sivaramakrishnan M, Stoica G, Wang LHV. Imaging of hemoglobin oxygen saturation variations in single vessels in vivo using photoacoustic microscopy. *Appl Phys Lett*. 2007; 90(5):053901.
49. Guo ZJ, Hu S, Wang LHV. Calibration-free absolute quantification of optical absorption coefficients using acoustic spectra in 3D photoacoustic microscopy of biological tissue. *Opt Lett*. 2010; 35(12):2067–2069. [PubMed: 20548388]
50. Lewis JS, Achilefu S, Garbow JR, Laforest R, Welch MJ. Small animal imaging: current technology and perspectives for oncological imaging. *Eur J Cancer*. 2002; 38(16):2173–2188. [PubMed: 12387842]
51. Weissleder R. Scaling down imaging: Molecular mapping of cancer in mice. *Nat Rev Cancer*. 2002; 2(1):11–18. [PubMed: 11902581]
52. Deroose CM, De A, Loening AM, Chow PL, Ray P, Chatziioannou AF, Gambhir SS. Multimodality imaging of tumor xenografts and metastases in mice with combined small-animal PET, small-animal CT, and bioluminescence imaging. *J Nucl Med*. 2007; 48(2):295–303. [PubMed: 17268028]
53. Gizurarson S. Animal-Models for Intranasal Drug Delivery Studies - a Review Article. *Acta Pharm Nordica*. 1990; 2(2):105–122.
54. Levine M, Tjian R. Transcription regulation and animal diversity. *Nature*. 2003; 424(6945):147–151. [PubMed: 12853946]
55. Buehler A, Herzog E, Razansky D, Ntziachristos V. Video rate optoacoustic tomography of mouse kidney perfusion. *Opt Lett*. 2010; 35(14):2475–2477. [PubMed: 20634868]
56. American Cancer Society. Hawaii Pacific Division., Cancer Research Center of Hawaii., Hawaii. Dept. of Health. Hawaii cancer facts and figures 2010: a sourcebook for planning and implementing programs for cancer prevention and control. Honolulu, HI: The Division; 2010. p. 61
57. Schopper D, de Wolf C. How effective are breast cancer screening programmes by mammography? Review of the current evidence. *Eur J Cancer*. 2009; 45(11):1916–1923. [PubMed: 19398327]
58. Berg WA, Gutierrez L, NessAiver MS, Carter WB, Bhargavan M, Lewis RS, Ioffe OB. Diagnostic accuracy of mammography, clinical examination, US, and MR imaging in preoperative assessment of breast cancer. *Radiology*. 2004; 233(3):830–849. [PubMed: 15486214]

59. Yang WT, Le-Petross HT, Macapinlac H, Carkaci S, Gonzalez-Angulo AM, Dawood S, Resetskova E, Hortobagyi GN, Cristofanilli M. Inflammatory breast cancer: PET/CT, MRI, mammography, and sonography findings. *Breast Cancer Res Tr.* 2008; 109(3):417–426.
60. Ermilov SA, Khamapirad T, Conjusteau A, Leonard MH, Lacewell R, Mehta K, Miller T, Oraevsky AA. Laser optoacoustic imaging system for detection of breast cancer. *J Biomed Opt.* 2009; 14(2):024007. [PubMed: 19405737]
61. Li, J.K.J. Series on bioengineering and biomedical engineering v 1. River Edge, NJ: World Scientific; 2004. Dynamics of the vascular system.
62. Hu S, Maslov K, Tsytarev V, Wang LV. Functional transcranial brain imaging by optical-resolution photoacoustic microscopy. *J Biomed Opt.* 2009; 14(4):040503. [PubMed: 19725708]
63. Hu S, Rao B, Maslov K, Wang LV. Label-free photoacoustic ophthalmic angiography. *Opt Lett.* 2010; 35(1):1–3. [PubMed: 20664653]
64. Jiao SL, Jiang MS, Hu JM, Fawzi A, Zhou QF, Shung KK, Puliavito CA, Zhang HF. Photoacoustic ophthalmoscopy for in vivo retinal imaging. *Opt Express.* 2010; 18(4):3967–3972. [PubMed: 20389409]
65. Silverman, RH.; Kong, F.; Lloyd, HO.; Chen, YC. Fine-resolution photoacoustic imaging of the eye. Oraevsky, AA.; Wang, LV., editors. San Francisco, California, USA: SPIE; 2010. p. 75640Y-75648.
66. Silverman RH, Kong F, Chen YC, Lloyd HO, Kim HH, Cannata JM, Shung KK, Coleman DJ. High-resolution photoacoustic imaging of ocular tissues. *Ultrasound Med Biol.* 2010; 36(5):733–742. [PubMed: 20420969]
67. Shahi P, Pineda I. Tumoral angiogenesis: Review of the literature. *Cancer Invest.* 2008; 26(1):104–108. [PubMed: 18181052]
68. American Cancer Society. Cancer facts & figures 2008. Atlanta, GA: American Cancer Society; 2008.
69. Staley J, Grogan P, Samadi AK, Cui H, Cohen MS, Yang X. Growth of melanoma brain tumors monitored by photoacoustic microscopy. *J Biomed Opt.* 2010; 15(4):040510. [PubMed: 20799777]
70. Zhang Y, Cai X, Choi SW, Kim C, Wang LV, Xia Y. Chronic label-free volumetric photoacoustic microscopy of melanoma cells in three-dimensional porous scaffolds. *Biomaterials.* 2010; 31(33):8651–8658. [PubMed: 20727581]
71. Guyton, AC. Textbook of medical physiology. Vol. xli. Philadelphia: Saunders; 1991. p. 1014
72. Hale GM, Querry MR. Optical-Constants of Water in 200-Nm to 200-Mum Wavelength Region. *Appl Optics.* 1973; 12(3):555–563.
73. Xu Z, Li CH, Wang LV. Photoacoustic tomography of water in phantoms and tissue. *J Biomed Opt.* 2010; 15(3):036019. [PubMed: 20615021]
74. Lloyd-Jones. Heart Disease and Stroke Statistics-2010 Update: A Report From the American Heart Association (vol 121, pg e46, 2010). *Circulation.* 2010; 121(12):E260–E260.
75. Wang B, Su JL, Amirian J, Litovsky SH, Smalling R, Emelianov S. Detection of lipid in atherosclerotic vessels using ultrasound-guided spectroscopic intravascular photoacoustic imaging. *Opt Express.* 2010; 18(5):4889–4897. [PubMed: 20389501]
76. Karpiouk, AB.; Wang, B.; Emelianov, SY. Integrated catheter for intravascular ultrasound and photoacoustic imaging. Oraevsky, AA.; Wang, LV., editors. San Francisco, California, USA: SPIE; 2010. p. 756408-756406.
77. Allen, T.J.; Hall, A.; Dhillon, A.; Owen, J.S.; Beard, P.C. Photoacoustic imaging of lipid rich plaques in human aorta. Oraevsky, AA.; Wang, LV., editors. San Francisco, California, USA: SPIE; 2010. p. 75640C-75648.
78. Zink D, Fischer AH, Nickerson JA. Nuclear structure in cancer cells. *Nat Rev Cancer.* 2004; 4(9):677–687. [PubMed: 15343274]
79. Stoscheck CM. Quantitation of Protein. *Methods in Enzymology.* 1990; 182:50–68. [PubMed: 2314256]
80. Yao D, Maslov K, Shung KK, Zhou Q, Wang LV. In vivo label-free photoacoustic microscopy of cell nuclei by excitation of DNA and RNA. *Opt Lett.* 2010; 35(24):4139–4141. [PubMed: 21165116]

81. Li L, Zemp RJ, Lungu G, Stoica G, Wang LV. Photoacoustic imaging of lacZ gene expression in vivo. *J Biomed Opt.* 2007; 12(2):020504. [PubMed: 17477703]
82. Kim C, Qin RG, Xu JS, Wang LV, Xu R. Multifunctional microbubbles and nanobubbles for photoacoustic and ultrasound imaging. *J Biomed Opt.* 2010; 15(1):010510. [PubMed: 20210423]
83. Wang XD, Ku G, Wegiel MA, Bornhop DJ, Stoica G, Wang LHV. Noninvasive photoacoustic angiography of animal brains in vivo with near-infrared light and an optical contrast agent. *Opt Lett.* 2004; 29(7):730–732. [PubMed: 15072373]
84. Menglin L, Jung-Taek O, Xueyi X, Geng K, Wei W, Chun L, Lungu G, Stoica G, Wang LV. Simultaneous Molecular and Hypoxia Imaging of Brain Tumors In Vivo Using Spectroscopic Photoacoustic Tomography. *Proceedings of the IEEE.* 2008; 96(3):481–489.
85. Kim C, Erpelding TN, Maslov K, Jankovic L, Akers WJ, Song LA, Achilefu S, Margenthaler JA, Pashley MD, Wang LHV. Handheld array-based photoacoustic probe for guiding needle biopsy of sentinel lymph nodes. *J Biomed Opt.* 2010; 15(4):046010. [PubMed: 20799812]
86. Yao JJ, Maslov K, Hu S, Wang LHV. Evans blue dye-enhanced capillary-resolution photoacoustic microscopy in vivo. *J Biomed Opt.* 2009; 14(5):054049. [PubMed: 19895150]
87. Hu S, Yan P, Maslov K, Lee JM, Wang LHV. Intravital imaging of amyloid plaques in a transgenic mouse model using optical-resolution photoacoustic microscopy. *Opt Lett.* 2009; 34(24):3899–3901. [PubMed: 20016651]
88. Muller RH, Mader K, Gohla S. Solid lipid nanoparticles (SLN) for controlled drug delivery - a review of the state of the art. *Eur J Pharm Biopharm.* 2000; 50(1):161–177. [PubMed: 10840199]
89. Brannon-Peppas L, Blanchette JO. Nanoparticle and targeted systems for cancer therapy. *Adv Drug Deliv Rev.* 2004; 56(11):1649–1659. [PubMed: 15350294]
90. Yang XM, Stein EW, Ashkenazi S, Wang LHV. Nanoparticles for photoacoustic imaging. *Wires Nanomed Nanobi.* 2009; 1(4):360–368.
91. Lu W, Huang Q, Geng KB, Wen XX, Zhou M, Guzatov D, Brecht P, Su R, Oraevsky A, Wang LV, Li C. Photoacoustic imaging of living mouse brain vasculature using hollow gold nanospheres. *Biomaterials.* 2010; 31(9):2617–2626. [PubMed: 20036000]
92. Pan DPJ, Pramanik M, Senpan A, Ghosh S, Wickline SA, Wang LV, Lanza GM. Near infrared photoacoustic detection of sentinel lymph nodes with gold nanobeacons. *Biomaterials.* 2010; 31(14):4088–4093. [PubMed: 20172607]
93. Wang, B.; Joshi, P.; Sapozhnikova, V.; Amirian, J.; Litovsky, SH.; Smalling, R.; Sokolov, K.; Emelianov, S. Intravascular photoacoustic imaging of macrophages using molecularly targeted gold nanoparticles. Oraevsky, AA.; Wang, LV., editors. San Francisco, California, USA: SPIE; 2010. p. 75640A-75647.
94. Cui HZ, Yang XM. In vivo imaging and treatment of solid tumor using integrated photoacoustic imaging and high intensity focused ultrasound system. *Med Phys.* 2010; 37(9):4777–4781. [PubMed: 20964197]
95. Weissleder R, Ntziachristos V. Shedding light onto live molecular targets. *Nat Med.* 2003; 9(1):123–128. [PubMed: 12514725]
96. Ntziachristos V, Razansky D. Molecular Imaging by Means of Multispectral Optoacoustic Tomography (MSOT). *Chem Rev.* 2010; 110(5):2783–2794. [PubMed: 20387910]
97. Fang H, Maslov K, Wang LV. Photoacoustic Doppler effect from flowing small light-absorbing particles. *Phys Rev Lett.* 2007; 99(18):184501. [PubMed: 17995411]
98. Sheinfeld, A.; Gilead, S.; Eyal, A. Time-resolved photoacoustic Doppler characterization of flow using pulsed excitation. Oraevsky, AA.; Wang, LV., editors. San Francisco, California, USA: SPIE; 2010. p. 75643N-75646.
99. Brunker, J.; Beard, P. Pulsed photoacoustic Doppler flowmetry using a cross correlation method. Oraevsky, AA.; Wang, LV., editors. San Francisco, California, USA: SPIE; 2010. p. 756426-756428.
100. Wei CW, Huang SW, Wang CR, Li PC. Photoacoustic flow measurements based on wash-in analysis of gold nanorods. *IEEE Trans Ultrason Ferroelectr Freq Control.* 2007; 54(6):1131–1141. [PubMed: 17571812]
101. Fang H, Wang LHV. M-mode photoacoustic particle flow imaging. *Opt Lett.* 2009; 34(5):671–673. [PubMed: 19252588]

102. Yao J, Maslov KI, Shi Y, Taber LA, Wang LV. In vivo photoacoustic imaging of transverse blood flow by using Doppler broadening of bandwidth. *Opt Lett*. 2010; 35(9):1419–1421. [PubMed: 20436589]
103. Yao JJ, Wang LHV. Transverse flow imaging based on photoacoustic Doppler bandwidth broadening. *J Biomed Opt*. 2010; 15(2):021304. [PubMed: 20459226]
104. Chen SL, Ling T, Huang SW, Won Baac H, Guo LJ. Photoacoustic correlation spectroscopy and its application to low-speed flow measurement. *Opt Lett*. 2010; 35(8):1200–1202. [PubMed: 20410966]
105. Guldiken RO, Balantekin M, Zahorian J, Degertekin FL. Characterization of dual-electrode CMUTs: Demonstration of improved receive performance and pulse echo operation with dynamic membrane shaping. *Ieee T Ultrason Ferr*. 2008; 55(10):2336–2344.
106. Homan, K.; Gomez, S.; Gensler, H.; Shah, J.; Brannon-Peppas, L.; Emelianov, S. Design and development of multifunctional contrast agents for photoacoustic imaging. Achilefu, S.; Raghavachari, R., editors. San Jose, CA, USA: SPIE; 2009. p. 71900I-71907.
107. Guo ZJ, Li CH, Song LA, Wang LHV. Compressed sensing in photoacoustic tomography in vivo. *J Biomed Opt*. 2010; 15(2):021311. [PubMed: 20459233]
108. Zhang C, Li C, Wang LV. Fast and robust deconvolution-based image reconstruction for photoacoustic tomography in circular geometry: experimental validation. *IEEE Photonics J*. 2010; 2(1):57–66. [PubMed: 20953277]
109. Patrickeyev, I.; Oraevsky, AA. Multiresolution reconstruction method to optoacoustic imaging. Oraevsky, AA., editor. San Jose, CA, USA: SPIE; 2003. p. 99-105.
110. Wang J, Liu T, Jiao SL, Chen RM, Zhou QF, Shung KK, Wang LHV, Zhang HF. Saturation effect in functional photoacoustic imaging. *J Biomed Opt*. 2010; 15(2):021317. [PubMed: 20459239]
111. Danielli A, Favazza CP, Maslov K, Wang LV. Picosecond absorption relaxation measured with nanosecond laser photoacoustics. *Appl Phys Lett*. 2010; 97(16):163701. [PubMed: 21079726]

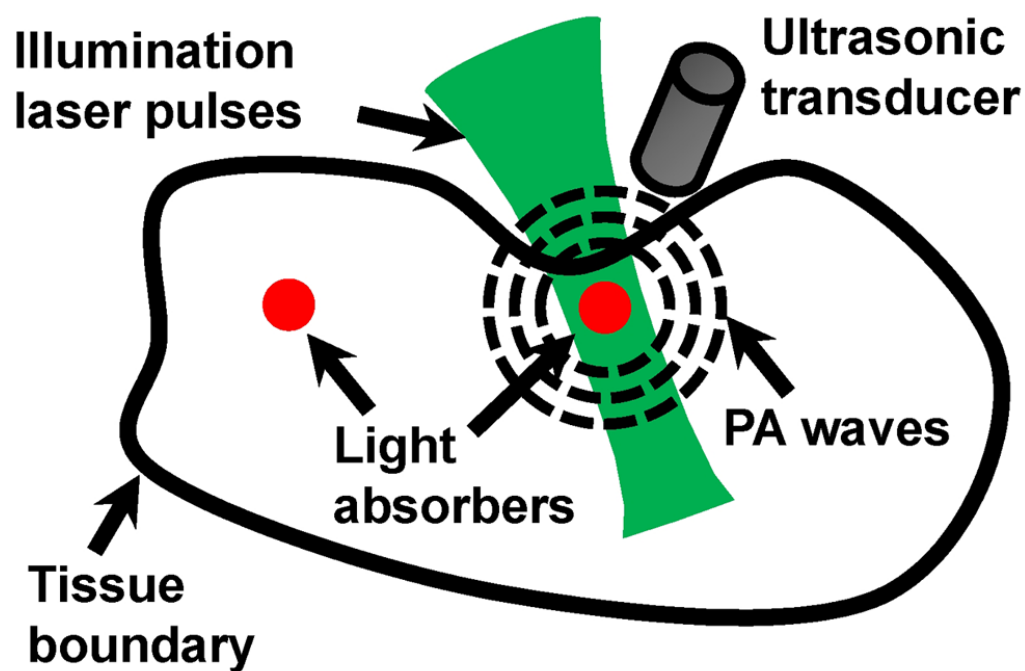


Figure 1.
Illustration of the photoacoustic (PA) effect and PA imaging

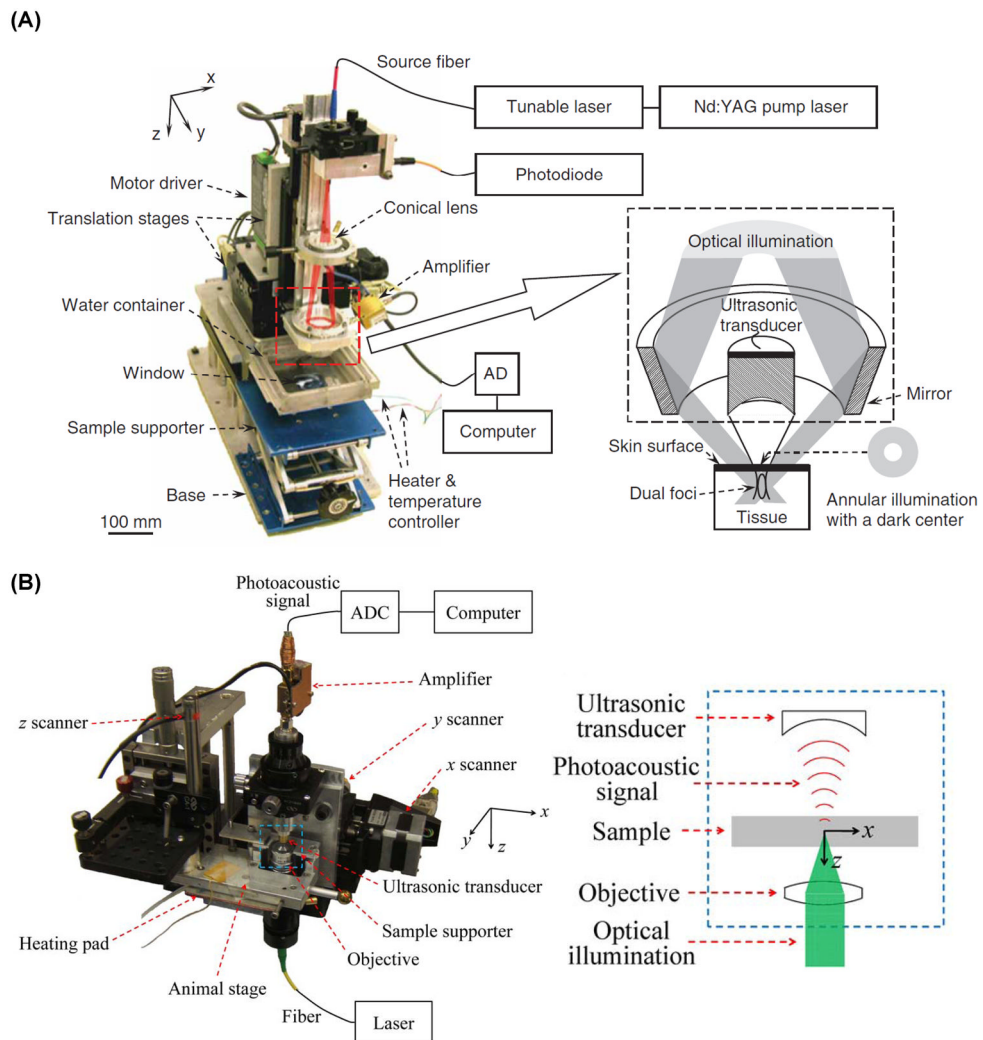


Figure 2. Raster-scan based photoacoustic microscopy (PAM)

(A) Schematic diagram of a dark-field acoustic-resolution photoacoustic microscope (AR-PAM). A transverse resolution of $15\ \mu\text{m}$ and axial resolution of $45\ \mu\text{m}$ are achieved, together with the maximum penetration depth of 3 mm in live animals. AD: analog-digital convertor. (B) Schematic diagram of an optical-resolution photoacoustic microscope (OR-PAM). Close-up: diagram showing the confocal alignment of the optical objective and the ultrasonic transducer. An organelle level resolution of $220\ \text{nm}$ has been achieved with a penetration depth of $200\ \mu\text{m}$. Reproduced with permission from Refs. (12,15).

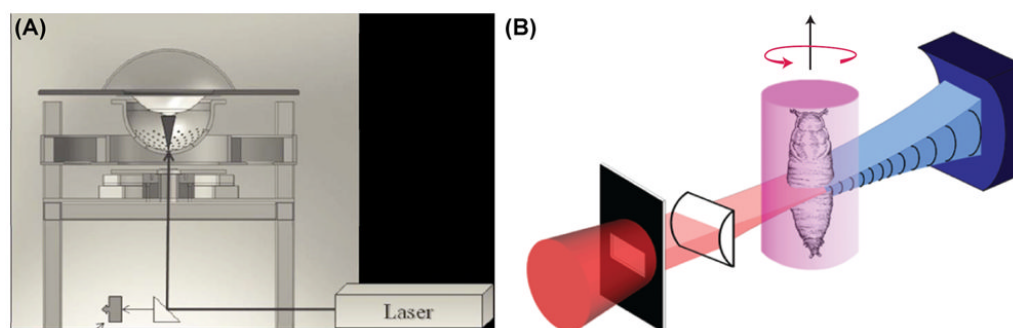


Figure 3. Inverse-reconstruction based photoacoustic computed tomography (PACT)

(A) Schematic diagram of a 128-element-based PACT system for human breast imaging using a hemisphere ultrasound array. Here, a $250\ \mu\text{m}$ spatial resolution over a $64\ \text{mm} \times 64\ \text{mm} \times 50\ \text{mm}$ field of view is achieved, and one volumetric image takes about 24 sec. (B) Schematic diagram of a multiwavelength photoacoustic tomography system using selective-plane illumination and a single element transducer. The sample is rotated to enable in-plane image reconstruction. Three-dimensional data acquisition is enabled by vertical scanning of imaging plane using a translational stage. Cross-sectional data acquisition normally takes 2 min at each wavelength. Red, illuminating light beam; blue, generated ultrasonic waves. Reproduced with permission from Refs. (24,25).

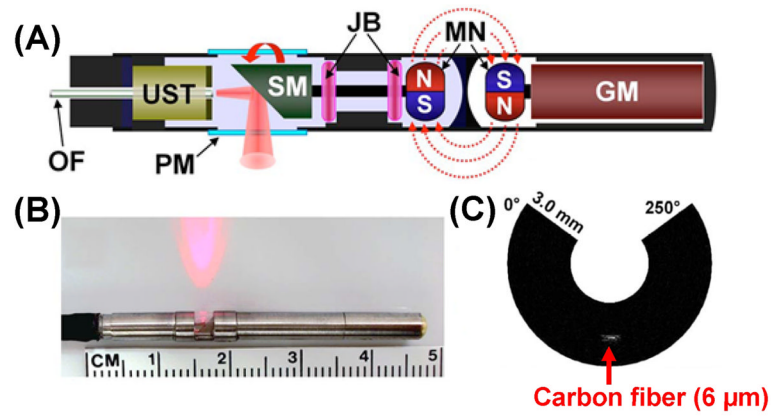


Figure 4. A photoacoustic endoscope with a miniaturized imaging probe
 (A) Schematic diagram of the photoacoustic endoscopic probe. GM, geared micromotor; JB, jewel bearings; MN, magnets; OF, optical fiber; PM, plastic membrane (imaging window); SM, scanning mirror; UST, ultrasonic transducer. (B) Photograph of the distal end of the probe with laser emitting through the central hole of the transducer. The probe diameter is 4.2 mm. (C) Photoacoustic endoscopic image of a carbon fiber (6 μm in diameter); polar coordinate representation. Reproduced with permission from Ref. (36).

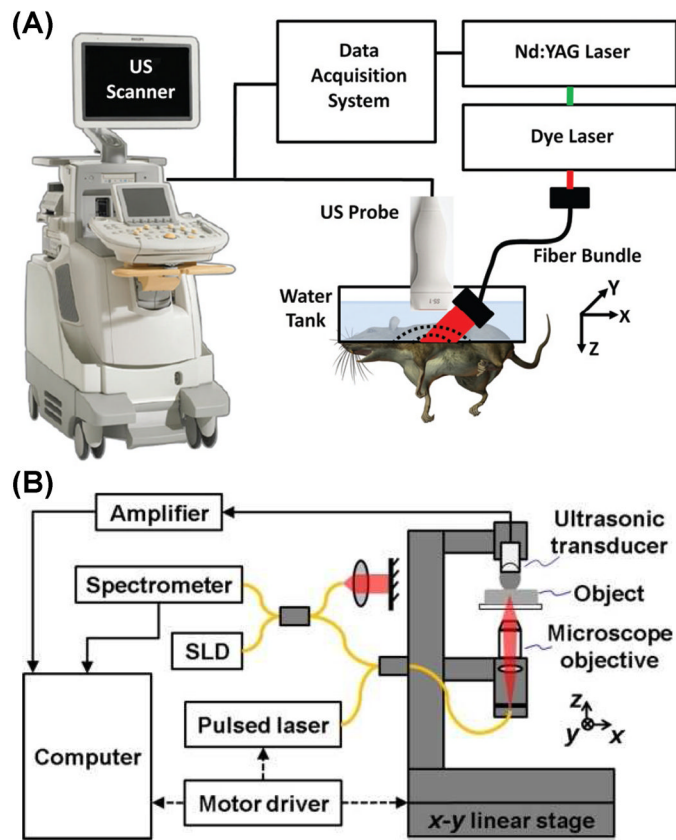


Figure 5. Hybrid systems combining PAT with other imaging modalities

(A) Experimental setup of a photoacoustic imaging combined with a clinical ultrasound (US) imaging system (iU22; Philips Healthcare). A fiber bundle is attached to the US probe for light delivery. The imaging plane of the US probe is coaxially aligned with the rectangular optical beam on the targeted area. (B) Schematic diagram of the combined photoacoustic and optical-coherence microscope. SLD, superluminescent diode. Solid lines represent single-mode optical fibers. Arrowhead solid lines show data flow. Arrowhead dashed lines show the flow of system control signals. Reproduced with permission from Refs. (38,39).

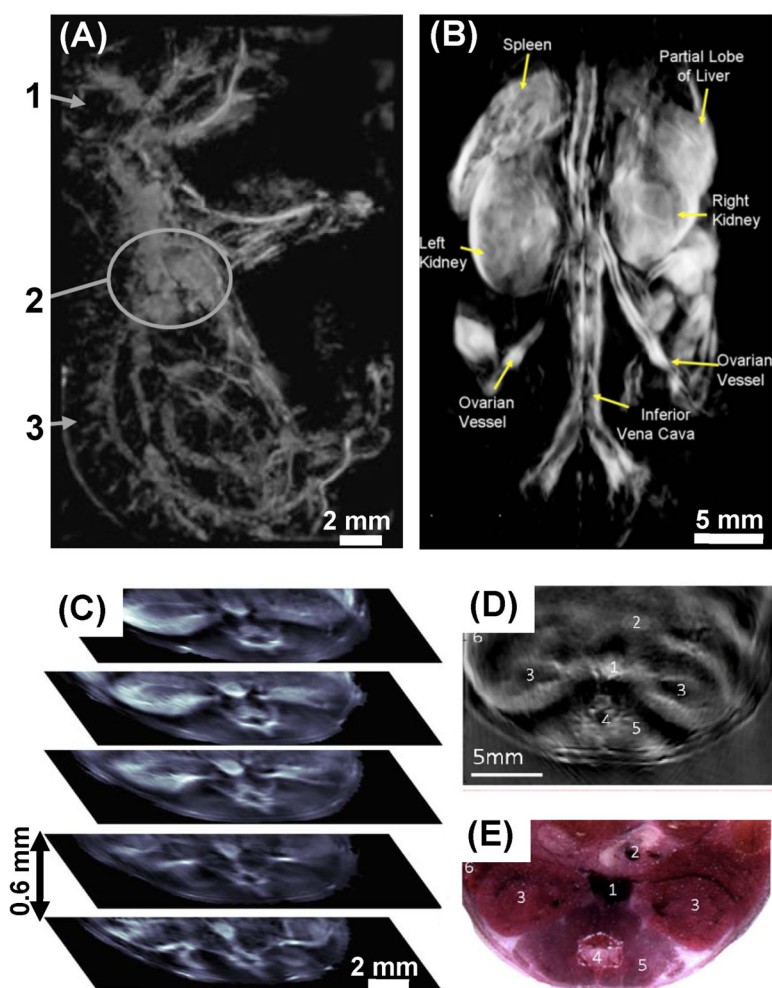


Figure 6. Whole-body photoacoustic tomography

(A) Vertical maximum amplitude projection of a 3D photoacoustic image (left) and photograph (right) of an *ex vivo* transgenic mouse embryo. 1, head; 2, heart region; 3, spinal region. (C) 3D whole-body photoacoustic image of a nude mouse. (C) Stack of representative slices of a 3D dataset of the pelvis and kidney region of a mouse. (D–E) Photoacoustic image (D) and photograph (E) of a cross-sectional slice. 1, vena cava; 2, portal vein; 3, kidneys; 4, spinal cord; 5, backbone muscles; 6, spleen. Reproduced with permission from Refs. (23,30,55).

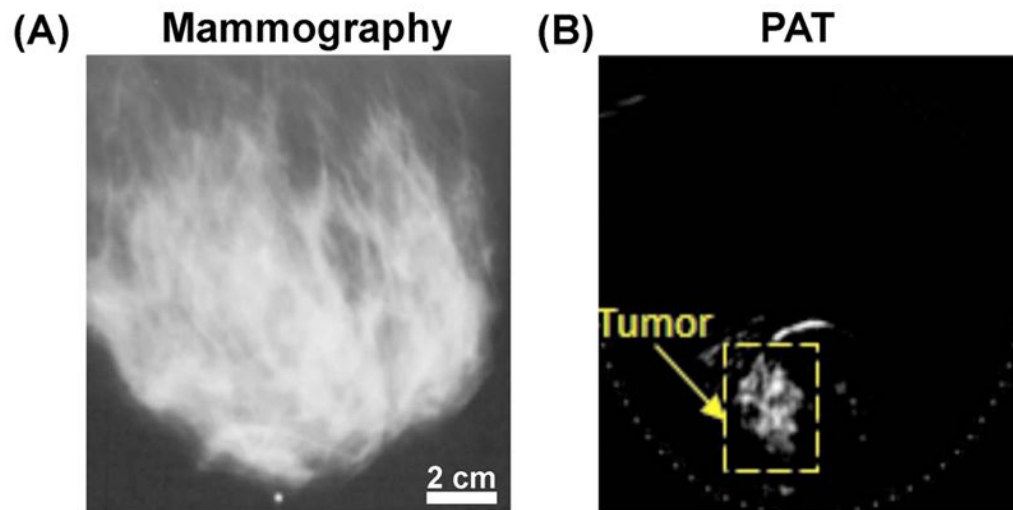


Figure 7. Photoacoustic tomography of human breast cancer
(A) Breast cancer image from mediolateral X-ray mammography. (B) Breast cancer image from mediolateral PAT. Reproduced with permission from Refs. (60).

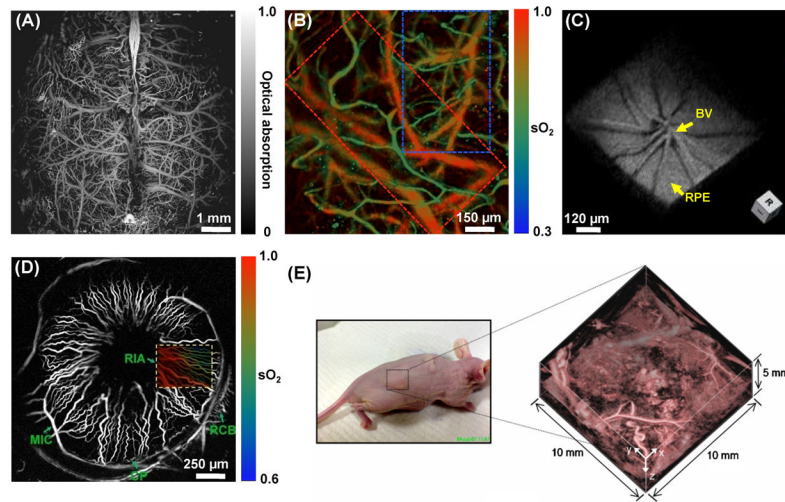


Figure 8. Photoacoustic tomography of microvasculature

(A) OR-PAM image of the mouse cortex vasculature with skull removed and scalp intact. (B) Oxygen saturation (sO_2) mapping of mouse brain microvasculature by OR-PAM. (C) Volumetric image of retinal structure of a rat by PA ophthalmoscopy (PAOM). BV, blood vessel; RPE, retinal pigment epithelium. (D) OR-PAM ophthalmic angiography of the iris microvasculature of a mouse, superimposed by the sO_2 mapping. CP, ciliary process; MIC, major iris circle; RCB, recurrent choroidal branch; RIA, radial iris artery. (E) FPI-PACT image of a human colorectal adenocarcinoma LS174T implanted under the skin of a nude mouse. Reproduced with permission from Refs. (9,31,62–64).

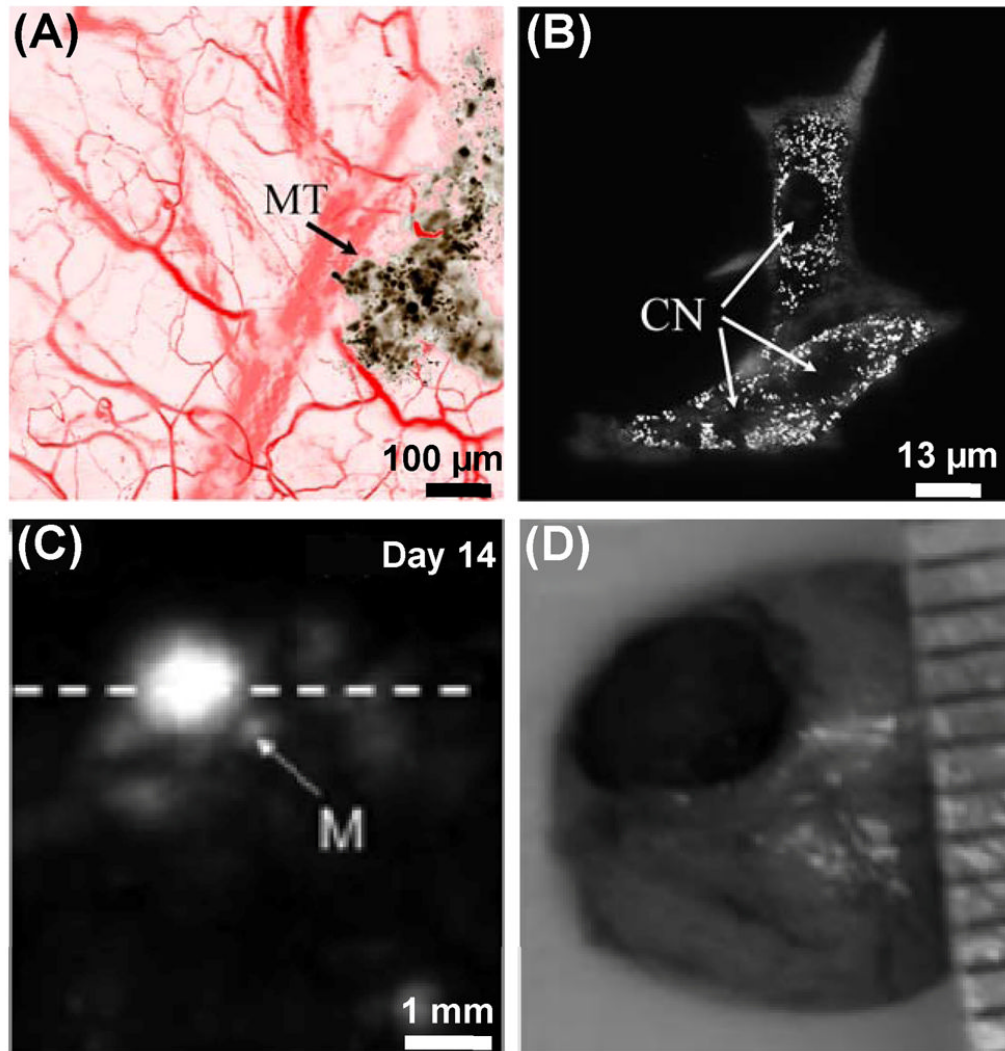


Figure 9. Photoacoustic tomography of melanin

(A) OR-PAM image of blood vessels (red) and melanoma (brown) taken four days after the injection of melanoma cells (NA of optical objective: 0.6). MT, melanoma tumor. (B) OR-PAM image of a single melanoma cell (NA of optical objective: 1.23). (C) Deep-reflection mode PAM image of a mouse brain taken 14 days after the injection of melanoma cells. (D) Invasive anatomical photograph after the mouse was sacrificed. M, brain melanoma. Reproduced with permission from Refs. (15,69).

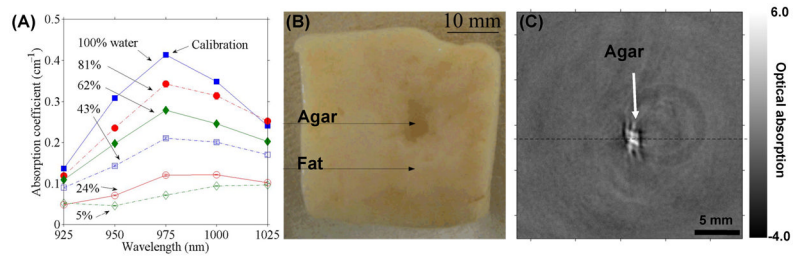


Figure 10. Photoacoustic tomography of water

(A) PA spectral measurements of water-ethanol mixtures at different water concentrations.

(B) Photograph of a tissue phantom made of fat with an embedded 2% agar object. (C)

Cross-sectional PACT image of the tissue phantom. Reproduced with permission from Ref. (73).

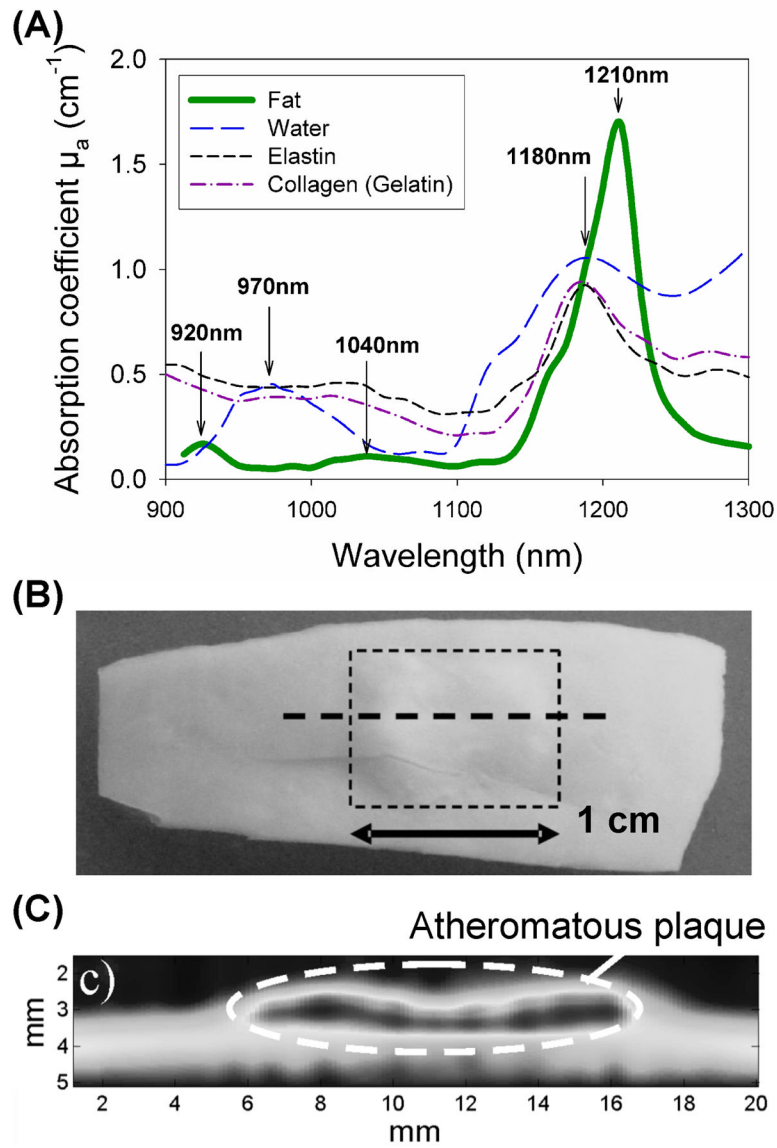


Figure 11. Photoacoustic tomography of lipid

(A) Optical absorption spectra of fat and other tissue components. (B) Photograph of an aorta sample with a raised lipid rich plaque (the horizontal dotted line represents the scan line). (C) Photoacoustic image obtained at 1200 nm when illuminating through saline. Reproduced with permission from Ref. (77).

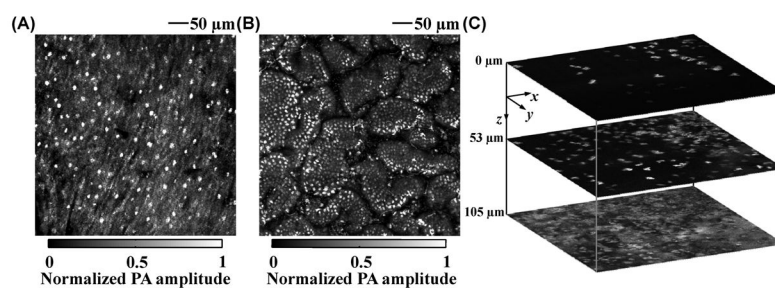


Figure 12. Photoacoustic tomography of cell nuclei

(A) UV-PAM image of cell nuclei of epithelia in the *ex vivo* lip of a mouse. (B) UV-PAM image of cell nuclei of epithelia in the *ex vivo* intestinal villi of a mouse. (C) *In vivo* UV-PAM images of cell nuclei in the ear skin of a nude mouse at depths of 0, 53, and 105 μm . Reproduced with permission from Ref. (80).

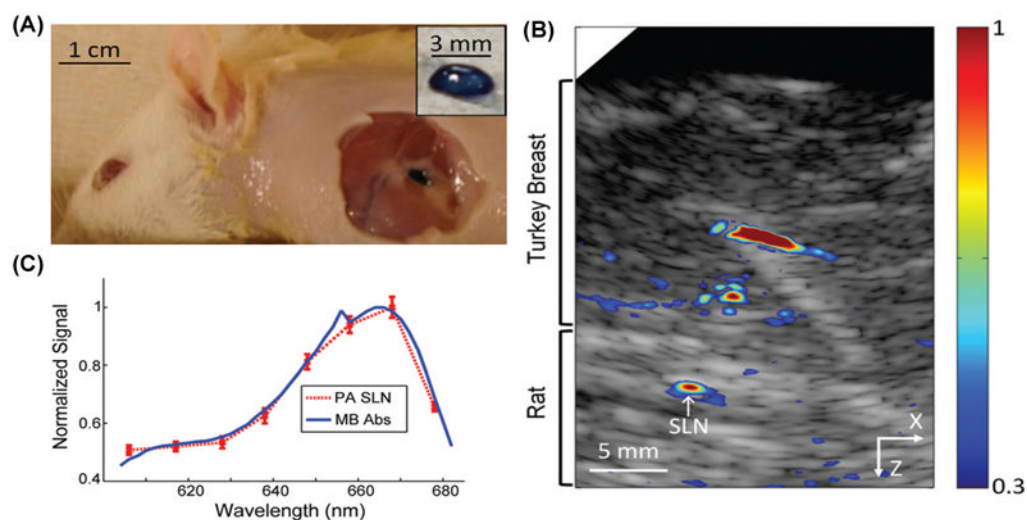


Figure 13. Photoacoustic tomography of sentinel lymph node (SLN) using methylene blue (MB) (A) Postmortem photograph of a rat acquired after PACT imaging and skin removal. Inset: dissected SLN stained by using MB. (B) Co-registered photoacoustic (in color) and ultrasound (in gray) B-mode images of rat SLNs acquired *in vivo* with a 2-cm thick turkey tissue layer for increased imaging depth. (C) Confirmation of MB accumulation in SLNs by spectroscopic PA imaging. Reproduced with permission from Ref. (38).

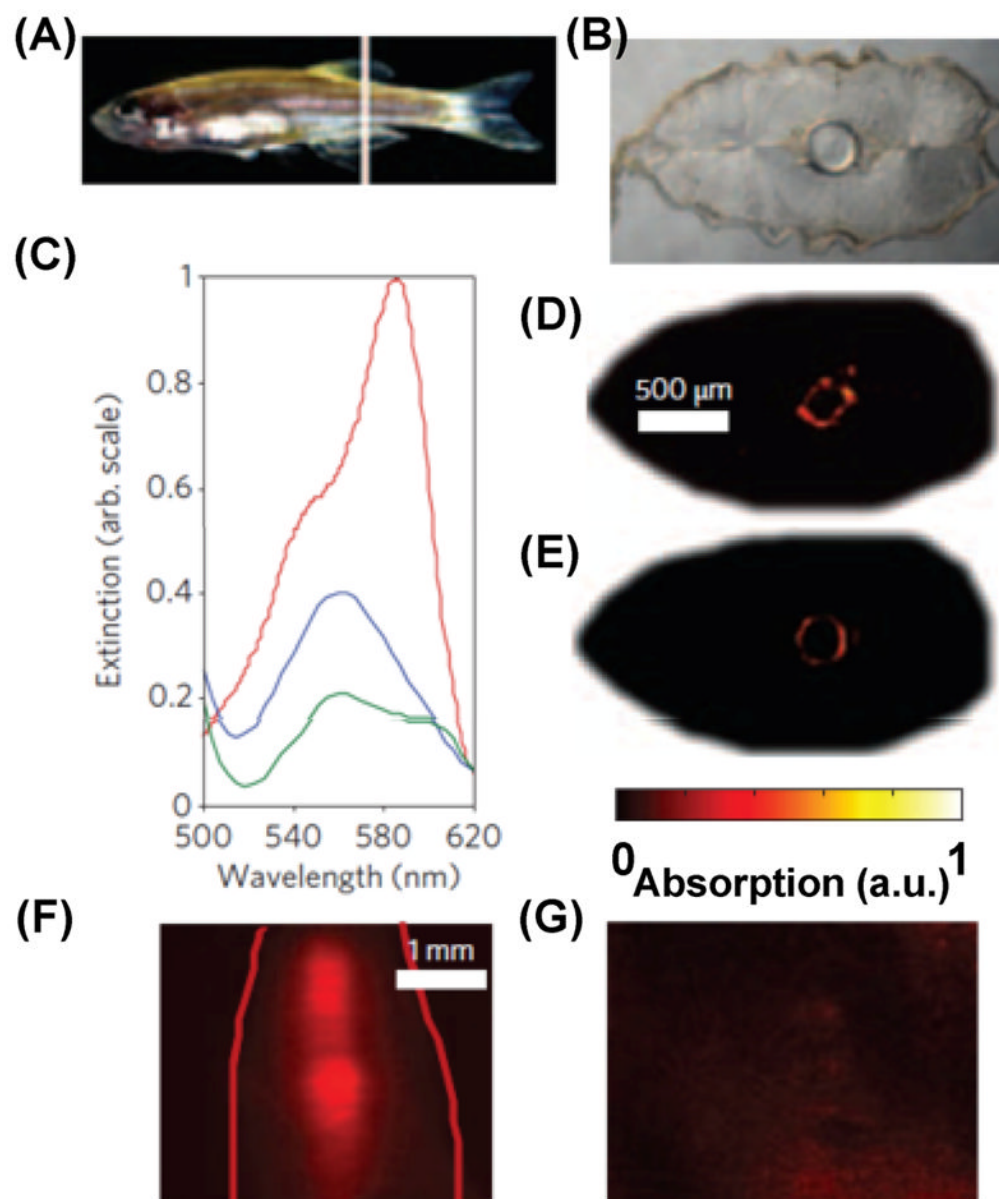


Figure 14. Photoacoustic tomography of deep-seated fluorescent protein mCherry of a zebrafish *in vivo*

(A) Photograph of an adult zebrafish. The solid line indicates the location of the imaging plane (the short axis thickness is 2.5 mm). (B) Regular histological section of the imaging plane. (C) Extinction spectra of mCherry (red) and the intrinsic background (blue, vertebral column; green, muscles). (D) Spectrally resolved PACT image of mCherry distribution in the intact animal. (E) Histological epifluorescence image of dissected tissue at approximately the same imaging plane (red color corresponds to mCherry-expressing vertebral column). (F) Epifluorescence image of a living zebrafish. Red curves show the surface outline. (G) Coronal confocal image at a depth of 500 μm from the surface. Reproduced with permission from Ref. (25).

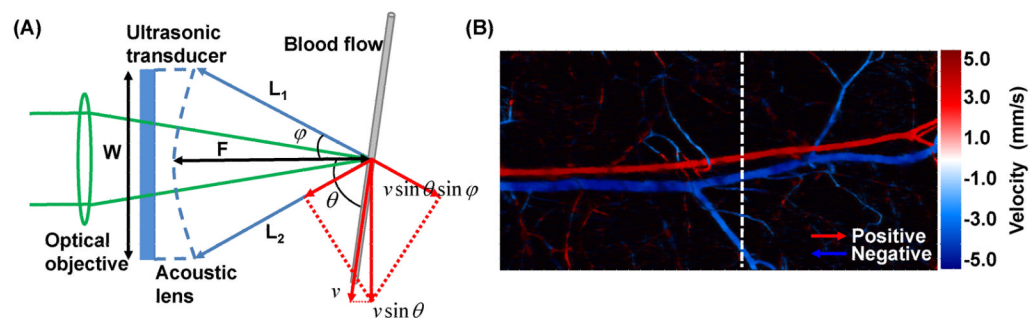


Figure 15. Photoacoustic tomography of blood flow using Doppler broadening of bandwidth (A) Beam geometry of PA Doppler bandwidth broadening. (B) PA imaging of blood flow in a mouse ear. The positive and negative flow directions are defined by the arrows. Reproduced with permission from Ref. (102).